Article

The Anisotropic Mechanical and Tribological Behaviors of Additively Manufactured (Material Extrusion) Implant-Grade Polyether Ether Ketone (PEEK)

Mohammad Reza Maydanshahi [1], Mohammad Reza Najari [2], Tom Slatter [2] and Mahdi Mohammadpour [2,*]

1   Department of Materials Science and Engineering, Ferdowsi University of Mashhad, Mashhad 91775, Iran; m.maydanshahi@mail.um.ac.ir
2   Wolfson School of Mechanical, Electrical and Manufacturing Engineering, Loughborough University, Loughborough LE11 3TU, UK; m.najjari-saadatabadi@lboro.ac.uk (M.R.N.); t.j.slatter@lboro.ac.uk (T.S.)
*   Correspondence: m.mohammad-pour@lboro.ac.uk

Abstract: In this study, we investigated the mechanical and tribological properties of the layer-by-layer structure of additively manufactured implant-grade Polyether Ether Ketone (PEEK) through the Material Extrusion (ME) process as a potential substitute for artificial joints. The effective elasticity modulus of the anisotropic 3D-printed PEEK was determined to be 2.505 GPa along the vertical and horizontal build orientations. The lubricated friction and wear performance were assessed using a pin-on-disk test under various loads, including 14, 30, 50, and 70 N, with a sliding speed of 50 mm/s over a total distance of 1 km at 37 °C. The contact parameters between the hemispherical steel pin and 3D-printed PEEK disks, involving contact pressures over the circle of contact, were observed to increase as the load increased. The results indicated that the wear coefficient exhibited a rise from 1.418×10^{-5} to 2.089×10^{-1} as the applied loads increased, signaling a shift from mild to severe wear regimes. Fetal Bovine Serum (FBS) as a lubricant exhibited a mixed mechanism, ascertained through the Stribeck curve, as well as a minimum fluid film thickness of 1.346 nm under an isoviscous–elastic regime, as calculated by the maximum load. Moreover, the mechanism governing wear during sliding, influenced by both normal axial and shear loads, primarily involved adhesion.

Keywords: additive manufacturing; polyether ether ketone; mechanical anisotropy; wear; lubrication

1. Introduction

Osteoarthritis is a degenerative joint condition that ranks as the fourth leading cause of global disability, characterized by the progressive deterioration of joint cartilage and underlying bone [1]. Its symptoms, including gradual joint pain, swelling, limited motion, and stiffness, predominantly affect the hands, spine, hips, and knees [2,3]. The most commonly used materials can be categorized into soft-on-hard and hard-on-hard combinations. Soft-on-hard combinations include ultra-high-molecular-weight polyethylene (UHMWPE), which is favored for acetabular cups and tibial components, against cobalt chromium alloys or alumina/zirconia toughened alumina composite ceramics (ZTA). The release of wear particles from metal-on-plastic artificial joints, particularly those incorporating UHMWPE, remains a significant concern in Total Joint Arthroplasty (TJA) failure [4]. The presence of microscale particles triggers a cascade of cytokine responses within the body, leading to osteolysis and aseptic loosening, potentially compromising the long-term success of TJA procedures [5]. Hard-on-hard bearing surface combinations for hip and knee joints include metal-on-metal, ceramic-on-ceramic, and ceramic-on-metal. In recent years, metal-on-metal artificial joint prostheses, utilizing materials such as titanium alloys, CoCrMo alloys, and stainless steel, have faced escalating concerns regarding the degradation of bone quality adjacent to these metallic prostheses and fracture fixation plates, increased wear when lubrication breaks down, fretting wear damage, and metallic corrosion on the

contact surfaces, significantly impacting revision rates and reducing the overall lifespan of artificial joints [6,7]. Furthermore, the generation of wear debris and the leaching of metal ions exert deleterious effects on surrounding tissues, giving rise to complications such as osteolysis, metal hypersensitivity, ion toxicity, and inflammatory or necrotic responses [8,9]. In routine clinics, ceramic-on-ceramic bearings like alumina and ZTA are preferred due to their excellent wear resistance, oxidation resistance, and toughness [10]. Nevertheless, ceramic-on-ceramic joints may encounter the occasional complications of squeaking, elevated fracture rates within zirconia femoral heads, and bio-inert properties which do not directly integrate with bone tissue [11]. Moreover, the high elastic modulus of these metals and ceramics leads to a substantial discrepancy between the requisite stress for bone tissue regeneration and the actual stress experienced by the surrounding bone near the implant. Consequently, the phenomenon of "stress shielding" ensues, leading to periprosthetic bone resorption and weakened bone around the implant, ultimately culminating in aseptic loosening and failure [12].

PEEK, with mechanical properties more akin to natural bone, is emerging as a promising replacement for UHMWPE, metal, and ceramic prostheses in applications like hip, knee, and spinal disc implants [13]. PEEK and its composites can be tailored to exhibit a wide range of properties, including non-toxicity, high-temperature resistance, corrosion resistance, abrasion resistance, a high strength, a high toughness, X-ray radiolucency, and an excellent sterilization performance, making them highly versatile for various orthopedic applications [14]. Extensive research demonstrates that PEEK-based wear particles, along with its abrasive particles, fall within an acceptable range for phagocytosis and exhibit a cytotoxicity comparable to UHMWPE controls due to its excellent biocompatibility [13,15]. The production of medical devices and implants has transformed with the advent of polymer filaments based on PEEK adhering to the standard specification for PEEK polymers for surgical implant applications such as ASTM F2026 [16]. Material Extrusion (MEX) additive manufacturing (AM) enables the production of PEEK prostheses intended for permanent use within the human body, offering notable advantages like cost effectiveness, rapid prototyping, and efficient end-use part creation [17]. MEX parameters include the layer thickness, raster angle, infill density, printing speed, and nozzle's temperature and diameter, which enormously affect the mechanical properties of the component. However, the build orientation parameter has the greatest effect on the anisotropic and mechanical behavior of 3D-printed components [18]. The anisotropic nature of 3D-printed components arises from the layer-by-layer fabrication method, affecting their inherent mechanical characteristics.

Moreover, at the molecular level, analogous phenomena such as anisotropic π–π stacking interactions, which play a role in superlubricity, highlight how controlled molecular orientation reduces friction. While π–π interactions may not be directly relevant to PEEK, the anisotropy introduced during layer-by-layer printing similarly affects its tribological performance [19].

The angle-dependent strength of chemical bonds further reflects the directional mechanical properties seen in AM PEEK, where the material's performance under loads varies with orientation. Anisotropic friction observed in systems like ligand–protein complexes underscores the importance of directional interactions in materials science. In AM PEEK, this manifests as directional variations in friction and wear due to differences in layer bonding and surface roughness [20,21].

Understanding these anisotropic behaviors is critical for optimizing AM PEEK in high-performance applications, where mechanical and tribological properties must be carefully controlled.

Evaluating the tensile and flexural properties of 3D-printed PEEK (Victrex® PEEK 450G, Lancashire, UK) using two distinct build orientations and unchanged parameters, including a nozzle temperature of 410 °C, bed temperature of 100 °C, layer height of 0.1 mm, nozzle diameter of 0.4 mm, and infill density of 100%, showed that the tensile modulus and strength of the horizontally printed samples were 3.54 GPa and 72.88 ± 1.92 MPa (at the point of fracture), respectively. These values for the vertically printed samples exhibited

a tensile modulus of 3.03 ± 0.01 GPa and a strength of 9.99 ± 0.94 MPa (at the point of fracture). In terms of flexural properties, the horizontally printed samples exhibited a flexural modulus of 3.06 ± 0.21 GPa and a strength of 124.3 ± 7.98 MPa. On the other hand, the vertically printed samples displayed a flexural modulus of 2.54 ± 0.07 GPa and a strength of 16.40 ± 2.18 MPa [22]. The compressive properties of the 3D-printed Victrex PEEK 450G specimens consisted of a modulus of 1.82 GPa and a strength of 102.38 MPa, employing nozzle temperatures ranging from 400 to 430 °C, a build temperature of 130 °C, an ambient temperature of 80 °C, a layer thickness of 0.2 mm, a raster width of 0.6 mm, and a fill density of 100% [23]. The mechanical properties of 3D-printed pure PEEK filaments (VESTAKEEP® i4G, Evonik Industries AG, Essen, Germany) through bending and compressive tests with horizontal and vertical build orientations, respectively, were determined. Consistent 3D-printing parameters included a layer thickness of 0.1 mm, a plate temperature of 250 °C, a 100% infill ratio, and a rectilinear infill pattern within a closed chamber. Variable parameters encompassed nozzle diameters of 0.2 mm, 0.4 mm, and 0.6 mm, nozzle temperatures of 420 °C, 430 °C, and 440 °C, and printing speeds of 5 mm/s, 10 mm/s, and 15 mm/s. The highest bending strength of 193.33 ± 7.04 MPa was obtained under using a 0.4 mm nozzle, a printing speed of 10 mm/s, and a nozzle temperature of 430 °C, alongside the lowest bending modulus of 1.049 ± 0.097 GPa. Similarly, the most favorable compressive results were attained with a 0.6 mm nozzle, a printing speed of 10 mm/s, and a nozzle temperature of 430 °C, yielding a compressive strength of 87.00 ± 1.02 MPa and an elastic modulus exceeding 2 GPa [24]. The study extensively investigated the mechanical properties of 3D-printed PEEK, including its tensile, compressive, and bending responses. However, the detailed analysis of the anisotropic and direction-dependent characteristics of MEX PEEK is in its early stages. This research aims to thoroughly examine the inherent mechanical properties of AM PEEK.

There are a lack of investigations on evaluating the wear behavior of 3D-printed PEEK, especially in terms of artificial joints arthroplasty applications. Therefore, the wear behavior of PEEK made with methods other than the AM process is studied for comparison with the 3D-printed PEEK.

Neat and nano-reinforced PEEK filaments (molding grade, Solvay) were synthesized using a laboratory filament extrusion system. These filaments incorporated carbon nanotubes (CNTs) and graphene nanoplatelets (GNPs). Disk-shaped specimens were 3D printed from PEEK and PEEK nanocomposite filaments and evaluated for their fretting wear behavior against a 6 mm AISI E52100 stainless steel ball (Washington, DC, USA). The ball-on-flat wear test involved a frequency of 5 Hz, an applied load of 10 N, and an amplitude of 100 μm over 10,000 cycles. The coefficient of friction (COF) decreased from approximately 0.25 (for neat PEEK) to 0.08 for the CNT/PEEK composite with a 1 wt.% CNT content and to 0.1 for the GNP/PEEK composite with 3 wt.% GNP content. This reduction in COF correlated with changes in material hardness. Wear rate analysis showed that the neat PEEK had the lowest wear rate at 1.23 mm^3 (Nm)$^{-1}$, while the PEEK samples reinforced with carbon nanostructures exhibited higher wear rates, specifically 2.97 mm^3 (Nm)$^{-1}$ for CNT/PEEK and 2.72 mm^3 (Nm)$^{-1}$ for GNP/PEEK [25]. An exploration into the simulation of artificial hemiarthroplasty was conducted, revealing distinct frictional characteristics. Specifically, the average coefficients of friction were determined as 0.095, 0.010, and 0.080 for PEEK, CoCrMo, and ceramic materials, respectively, in articulation with cartilage. This assessment transpired over a sliding duration ranging from 10 to 30 min, governed by a sliding velocity of 2 mm/s and subject to a contact stress of 1 MPa. Remarkably, the PEEK/cartilage interface showcased minimal surface deterioration, featuring a notably smooth surface with limited detachment. This outcome can be attributed to the marked differences in the hardness, strength, and modulus of elasticity between ceramics, CoCrMo, and PEEK [26]. The self-prepared CFR-PEEK composite, in cylindrical pin form, exhibited an average specific wear rate of 0.93 ± 0.30 × 10^{-7}mm^3 (Nm)$^{-1}$ when articulated against smooth alumina ceramic surfaces in pin-on-plate multidirectional tribometry. This evaluation employed lubrication with 25% (*v/v*) bovine serum in sterile

water, a 5 km sliding distance, a 160 N load, and a 120° pin rotation angle per cycle. Notably, the CFR–PEEK composite showed a lower volumetric wear compared to polyethylene, with a wear factor of $2.00 \pm 0.50 \times 10^{-7} \text{mm}^3 \, (\text{Nm})^{-1}$ against CoCr [27].

In order to investigate the tribological behavior of 3D-printed PEEK intended to be an artificial joint dominantly experiencing a compression situation, the anisotropic compressive behavior of the 3D-printed PEEK was primarily determined with respect to the vertical and horizontal build orientations (Figure 1). These two build orientations identified two layer orientations, which were perpendicular and parallel to the compressive load direction. The six elastic constants derived from compressive tests served as the basis for determining the reduced Young's modulus of the anisotropic 3D-printed component using a stiffness matrix. The contact parameters of the 3D-printed PEEK polymer disk articulated against a non-conformal spherical metal pin in the tribology experiment were investigated based on the Hertz criterion of elasticity theory.
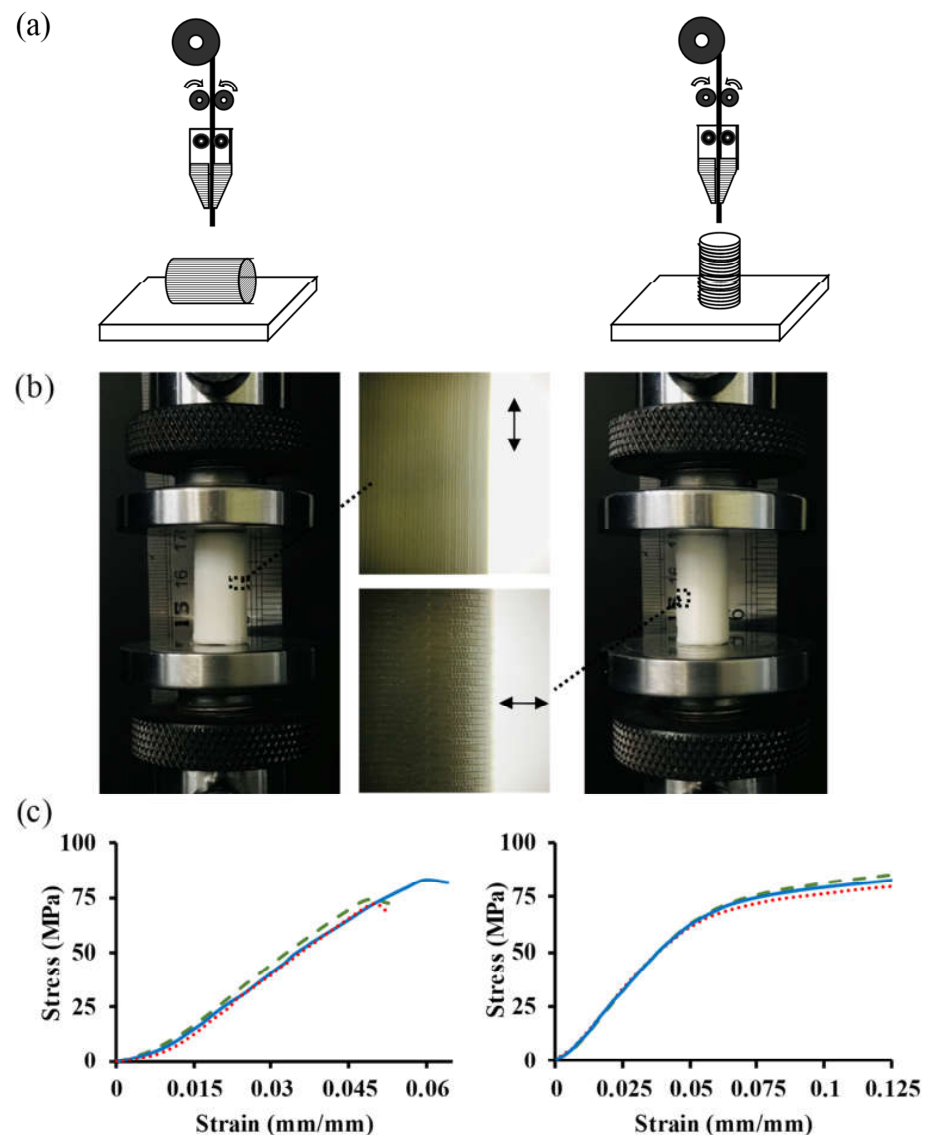

Figure 1. (**a**) Schematic of additive manufacturing of PEEK filament in the horizontal build orientation (**left**), and the vertical build orientation. (**b**) The uniaxial compressive test machine for assessing compression behavior of the horizontal build orientation (**left** and **middle-up**), and the vertical build orientation (**right** and **middle-down**). (**c**) Stress–strain graph of the 3D-printed PEEK subjected to the compressive load parallel to the deposited layer direction (**left**), and perpendicular to the deposited layer direction (**right**).

The deformation of 3D-printed PEEK under the tribology circumstance may be either plastic or elastic, depending on the magnitude of the applied load, which was also examined based on the Tresca and Huber–Mises criteria of plasticity theory. The wear coefficients (K) of the 3D-printed PEEK were determined as material properties in the mild and severe wear regimes. Moreover, the specific wear rates (k) of the 3D-printed components werer calculated by varying the loads. In order to match the clinical results of the 3D-printed PEEK with the in vitro experiment, Fetal Bovine Serum (FBS) was selected as a lubrication in the tribology test, and the lubrication mechanism was evaluated through the Stribeck curve. Furthermore, the lubrication mechanism was also determined by calculating the minimum film thickness of the lubricant by varying the loads.

This research defines a new procedure for optimizing the tribological aspects of artificial joint replacement interventions by determining the anisotropic mechanical properties of 3D-printed implant-grade polymers used as bearing surfaces for human total joint prostheses. This optimization aims to mitigate the occurrence of aseptic loosening and failure in total joint arthroplasty, phenomena primarily attributed to adhesion, two- or three-body abrasion, and surface fatigue wear mechanisms. Additionally, a significant gap is evident in the current literature regarding the examination of the influence exerted by the mechanical anisotropy properties and inherent porosity of additively manufactured components on wear and lubrication behaviors. This omission is particularly noteworthy, given the striking resemblance between the lubrication dynamics of such porous components and those observed within articular cartilage.

2. Materials and Methods

2.1. Mechanical Properties

The compressive mechanical properties of 3D-printed PEEK were determined in the two build orientations of longitudinal and transverse due to the anisotropy behavior of AM components caused by the layer-by-layer material deposition process of MEX. The compressive behavior of the 3D-printed PEEK based on the direction of its deposited layers to the applied load was investigated through the ASTM D695 incorporated into the standard test method for the compressive properties of rigid plastics. Specimens of 3D-printed PEEK (VESTAKEEP®i4 G) were fabricated by the 3D-printer (Apium P220, Karlsruhe, Germany) in the form of a right cylinder through longitudinal (horizontal) and transverse (vertical) build orientations with respect to the compressive load direction. The 3D printing parameters employed included a printing speed of 1500 mm/min, layer height of 0.1 mm, nozzle diameter of 0.4 mm, 100% infill, and raster angle of 0/90 degree, as detailed in Table 1. These parameters were meticulously selected based on their applicability and adherence to the established best practices found in the literature [24,28]. It is important to note that altering any of these parameters can significantly influence the mechanical properties of additively manufactured components. Generally, opting for lower printing speeds, thinner layer thicknesses, smaller nozzle diameters, and higher infill density percentages tends to enhance these mechanical properties. Furthermore, variations in raster orientations can yield disparate results due to the orientation of the raster lines relative to the applied load direction [29]. The specimens with a diameter size of 12.7 mm by 25.4 mm underwent the compression test using the Santam Universal Testing Machine (STM-150) (Teheran, Iran) with a displacement rate of 1.3 mm/min and a 2000 Kgf load cell capacity. The longitudinal build orientation samples were subjected to a load parallel to the layer deposition, and the transverse build orientation samples were subjected to a load perpendicular to the layer deposition. Calibrated axial and lateral extensometers were attached to each specimen to measure the displacement in two directions for calculating the Poisson's ratio. The average elastic modulus and yield strength for the both build orientations were determined through a stress–strain graph generated from the compressive test.

Table 1. Additive manufacturing parameters selected for both the mechanical and tribological tests.

Nozzle Temperature [°C]	Bed and Chamber Temperature [°C]	Nozzle Diameter [mm]	Layer Height [mm]	Raster Angle [°]	Printing Speed [mm/min]	Infill Density [%]	Cooling Fan [%]	Outline Shells
410	120	0.4	0.1	0/90	1500	100	0	2

2.2. Tribological Properties

The tribological properties of the 3D-printed PEEK were evaluated through the ASTM F732 incorporated into the standard test for the wear of polymeric materials used in total joint arthroplasty.

The ASTM F732 was proposed to evaluate material combinations for potential use as bearing surfaces in human total joint prostheses. The aim is to rank materials based on their polymer wear rates under simulated physiological conditions, using prototype prostheses in a joint simulator apparatus before clinical trials. These tests provide a cost-effective and reliable means for screening material combinations for their wear performance across various orthopedic applications, offering practical insights into wear behavior. Tribological investigations of polymeric materials for joint replacement involve various apparatuses, including ball-on-disk and pin-on-disk setups, as well as simulators akin to the hip or knee joints outlined in ASTM F732. Standardized procedures, following ASTM G-99 specifications for pin-on-disk tests, were employed for specimen preparation and wear characteristic calculations.

The 3D-Printed PEEK (VESTAKEEP®i4 G) specimens in the form of round disks were fabricated by the 3D printer (Apium P220) with inner and outer diameters of 5 and 40 mm, respectively, and a thickness of 2 mm. The 3D printing parameters were characterized by a printing speed of 1500 mm/min, layer height of 0.1 mm, nozzle diameter of 0.4 mm, 100% infill, horizontal build orientation, and raster angle of 0/90 degree, as detailed in Table 1. The wear test was carried out using pin-on-disk tribometer in a Fetal Bovine Serum (FBS) lubrication (Biochrome®, Berlin, Germany), with the 30–45 gL^{-1} protein concentration at a 37 ± 2 °C analogy to the human synovial joints and temperature. The specimens were rinsed prior to and after the wear test in an ultrasonic cleaner (Rocker®, Soner 203H, Taiwan (R.O.C.)) in distilled water, with a frequency of 53 KHz and a power of 100 W for 15 min, in order to detach any extraneous material that might affect the accuracy of the measurement. Afterward, the specimens were put in a dust-free and air-dry environment at room temperature for 24 h.

All specimens were weighed before and after the wear test and after the cleaning and drying processes by using a balance with a sensitivity of 0.0001 g (AND® GR-200 series, Tokyo, Japan).

A pin in ball shape made of high-carbon anti-friction 52,100 bearing steel (with a high wear resistance and rolling fatigue strength) was used based on the ASTM A295 standard in the tribology test. The pin used had a 6 mm diameter with the hardness and roughness of a 62 Rockwell hardness and 113 nm, respectively. The selected diameter of the pin provided the appropriate average contact area in the 3D-printed PEEK disks, as detailed in Table 4. Based on ASTM F732, in the context of reciprocating sliding, wherein a metal pin interacts with a flat polymer configuration, contact stresses exhibit spatial and temporal variations, attributed to Hertzian stress distribution and material deformation. Establishing a baseline for testing requires determining the appropriate load and corresponding contact stress. Calculations of the initial peak Hertzian contact stress and initial average contact stress are essential. For example, in the case of a CoCr pin bearing on a UHMWPE disk, initial average contact stress ranges from 19 to 24 MPa were reported. The difference in the average contact area may stem from variations in the mechanical properties of the chosen steel pin and 3D-printed PEEK compared to the CoCr pin and UHMWPE, as documented in ASTM F732.

The pin was stationary during the wear test under vertical loads of 14, 30, 50, and 70 N in each test. However, the 3D-printed discs rotated in a circular motion path with a diameter of 8 mm, at 120 rounds per minute or a sliding speed of $\approx$50 mm/s, with a sliding distance of 1000 m.

3. Results and Discussions

3.1. Mechanical Assessment

The mechanical properties of the AM of polymers are recognized as an anisotropic behavior caused by the layer-by-layer material deposition process of ME [30]. Therefore, the mechanical properties of the 3D-printed specimens, including the Young's modulus, yield strength, and Poisson ratios in two different build orientations, were determined, varying their physical properties relative to the direction. Although some mechanical properties of as-printed VESTAKEEP®i4 have been reported by the manufacturer, there are many aspects of 3D printing parameters and also different loading directions, with respect to the positioning of the layers due to the anisotropic behavior of the 3D-printed part, that influence the mechanical and tribological properties significantly [31]. The results gained from the compression test led to an elastic modulus of 2.30 ± 0.10 GPa and a yield strength of 61.0 ± 1.0 MPa, where the load direction was perpendicular to the layer direction, while an elastic modulus of 2.30 ± 0.2 GPa and a yield strength of 76.0 ± 7.0 MPa were obtained where the load direction was parallel to the layer direction. The Poisson's ratio was determined as the ratio of lateral to longitudinal strain obtained from the displacements of the extensometers according to Equation (1), where D is the length along the transverse axis and L is the length along the longitudinal axis.

$$\vartheta = -\frac{\frac{\Delta D}{D}}{\frac{\Delta L}{L}} \tag{1}$$

3.1.1. Anisotropy Behavior of 3D-Printed PEEK

The physical properties of the 3D-printed PEEK specimens were classified as transversely isotropic, wherein the *z*-axis of symmetry was perpendicular to the deposition layers, while the x-y plane of isotropy aligned parallel to the deposition layers [22,32].

The elasticity modulus and Poisson's ratio were obtained by the compression test directly; however, the shear modulus was determined by the Saint-Venant principle in Equation (2), which is a valid approximation for components with a low degree of anisotropy [33].

$$\begin{cases} \frac{1}{G} = \frac{2(1+v)}{E} \\ \frac{1}{G'} = \frac{1}{E} + \frac{1+2v'}{E'} \end{cases} \tag{2}$$

The six engineering constants of the transversely isotropic 3D-printed PEEK were measured based on the stiffness matrix and Hook's law (Table 2) [34,35].

Table 2. Six engineering constants of transversely isotropic 3D-printed PEEK.

	C1	C2	C3	C4	C5	C6
Elastic constants [GPa]	2.846	1.141	1.156	3.011	0.885	0.853

Transversely isotropic media exhibit exactly the same behavior as isotropic media. The only required change involves inserting the effective elasticity modulus [35]. Finally, the

effective elasticity modulus of the transverse isotropic 3D-printed PEEK can be written as in Equation (3) [36].

$$E^* = E_{Disk} = \frac{2 \times \sqrt{C_{44}} \times (C_{11}C_{33} - C_{13}^2)}{\sqrt{C_{11}} \times \sqrt{(\sqrt{C_{11}C_{33}} - C_{13}) \times (\sqrt{C_{11}C_{33}} + 2C_{44} + C_{13})}} \tag{3}$$

3.1.2. Contact Area

The adhesive normal contact area of the 3D-printed PEEK can be reduced to the equivalent non-adhesive contact problem, and is congruous with the isotropic material in terms of the contact problem. Redefining the effective elasticity modulus plays a crucial role in solving the contact problem of transverse isotropic material [35].

The geometry of contact in the tribology experiment was a circular contact area, which was between the flat surface of the 3D-printed disk and the spherical surface of the 52100 steel pin. The reduced radii of curvature and reduced Yong modulus were determined in Equations (4) and (5), respectively, in order to calculate the contact parameters [37,38].

$$\begin{cases} \frac{1}{R'} = \frac{1}{R_x} + \frac{1}{R_y} = \frac{1}{R_{Pin_x}} + \frac{1}{R_{Disk_x}} + \frac{1}{R_{Pin_y}} + \frac{1}{R_{Disk_y}} \\ R_{Disk_x} = R_{Disk_y} = \infty \\ R_{Pin_x} = R_{Pin_y} = R_{Pin} \end{cases} \tag{4}$$

$$E'' = \frac{2}{\left(\frac{1 - v_{Pin}^2}{E_{Pin}} + \frac{1 - v_{Disk}^2}{E_{Disk}} \right)} \tag{5}$$

The reduced radii of curvature R' was 1.5 mm, since the flat surface had infinite radii of curvature and the ball-shaped pin had a radius of 3 mm. The reduced Yong modulus was 5.403 GPa, where $E_{pin} = 200$ Gpa and $\vartheta_{pin} = 0.30$ were the elasticity modulus and Poission ratio of the pin, and $E_{disk} = 2.505$ Gpa and $\vartheta_{disk} = 0.29$ were the elasticity modulus and Poission ratio of the 3D-printed disk, respectively. The E'' and R' were the constant parameters during the tribology test, and the load (F) was 14, 30, 50, and 70 N. Then, the radius of the circular contact area was calculated through Equation (6).

$$r = \left(\frac{3FR'}{E''} \right)^{\frac{1}{3}}. \tag{6}$$

Afterward, the maximum and average contact pressures over the circle of contact (Figure 2b), maximum deflection, and the position of maximum shear stress below the center of the circle of contact were obtained according to Equations (7) and (8), respectively [39].

$$\begin{cases} P_{max} = \frac{3 \times F}{2 \times \pi \times r^2} \\ P_{ave} = \frac{F}{\pi \times r^2} \end{cases} \tag{7}$$

$$z = 0.638 \times r \tag{8}$$

The contact parameters for this tribology test were calculated according to the formulae summarized in Table 3.

Table 3. Contact parameters of 3D-printed PEEK indented by a hemispherical metal pin.

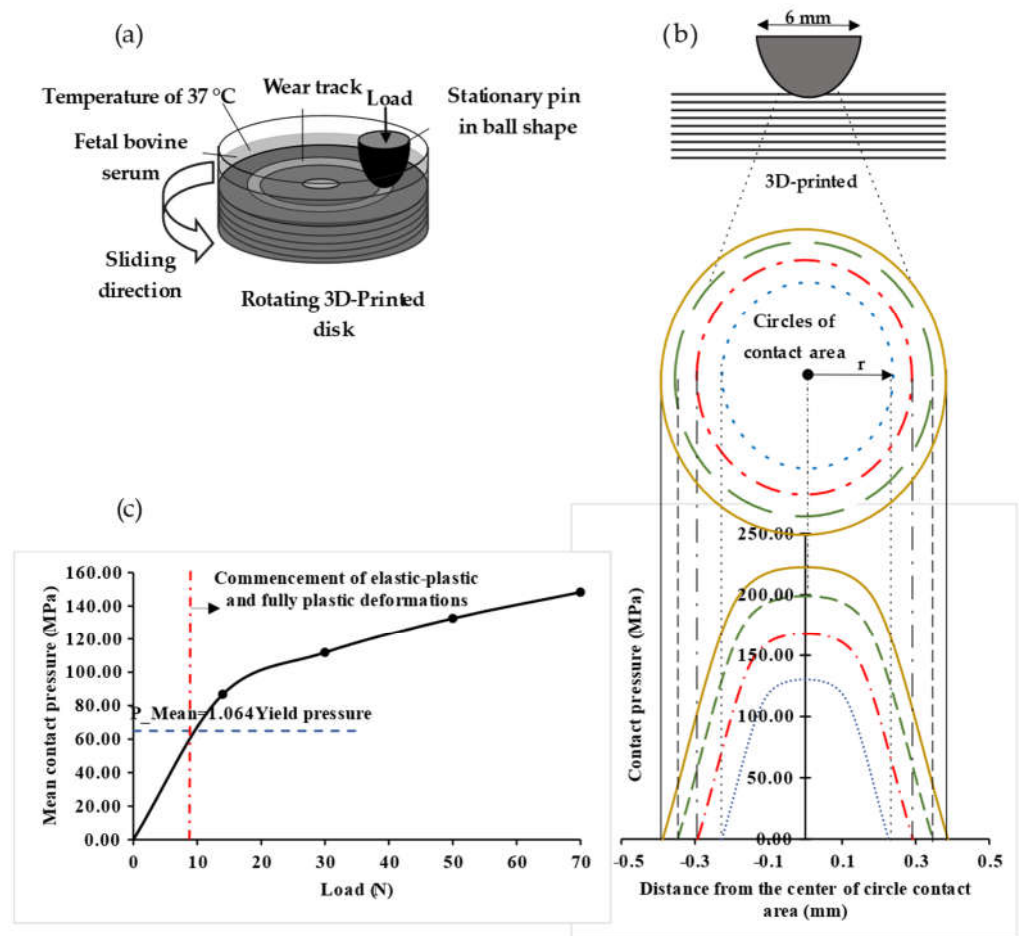| Load [N]	Radius of Circular Contact Area [mm]	Average Contact Pressures [MPa]	Maximum Contact Pressures [MPa]	Maximum Deflection [mm]	Depth of Maximum Shear Stress [mm]
14	0.227	86.708	130.063	0.017	0.145
30	0.292	111.787	167.681	0.028	0.186
50	0.346	132.538	198.808	0.040	0.221
70	0.388	148.269	222.404	0.050	0.247

Figure 2. (**a**) Schematic diagram of the pin-on-disk tribometer, (**b**) contact pressure distribution over circle of contact by load was varied from 14 N to 70 N, the inner circle correspond to the former, and the outer circle correspond to the latter, and (**c**) indentation mean contact pressure as a function of load for the surface of a 3D-printed specimen with yield stress of 58 MPa pressed by a hard stainless steel ball of diameter of 6 mm.

3.1.3. Elastic and Plastic Behavior

The deformation behavior of a softer disk material interacting with a harder spherical material acting as a pin can be classified into the following three regions: elastic, elastic–plastic, and fully plastic. This categorization depends on the applied load's magnitude and the hardness of the materials. This pin-on-disk test shares similarities with the indentation test studied by Tabor [40]. Although the deformation behavior of thermoplastic polymers is generally described as a viscoelastic solid due to the dependency of their elastic modulus and yield stress on the deformation rates, their indentation behavior can be characterized as resembling metals [41]. Based on the Tresca and Huber–Mises criteria, plastic deformation initiates when the shear stress equals half of the yield strength due to the equivalent radial stresses at this point. Therefore, plastic flow occurs when 0.47 times the mean contact pressure (P_{mean}) equals 0.5 times the yield strength (Y), as follows in Equation (11).

$$P_{mean} = 1.064 \times Y \tag{9}$$

The data in Figure 2c indicate that the pressure load characteristic of a spherical metal pin penetrating the 3D-printed polymer did not follow the characteristic observed when two metals were subjected to each other. The ratio of the mean contact pressure to the yield strength ($c = P_{mean}/Y$) can serve as a criterion for interpreting elastic and plastic behaviors. For the metal-on-metal articulation, for the portion below 1.064, the deformation

remained elastic, while for the portion between 1.064 and 2.8, the deformation was in the elastic–plastic state. Moreover, for the portion exceeding 2.8, the deformation became fully plastic. This dissimilar behavior may have been caused by the difference in the ratio of the elastic modulus to Young's modulus between thermoplastic polymers (in the order of 10) and metals (in the order of 100 to 1000) [31].

The graph of the mean contact pressure versus the load of the 3D-printed PEEK polymer, presented in Figure 2c, displays elastic–plastic deformation in regions with ratios 1.068, which correspond to the area allocated to the metals [40]. The region of elastic–plastic behavior is not as distinct as it is for metals, and the graph transitions into the fully plastic region shortly after the elastic region.

3.2. Tribological Assessment

Tribology evaluations incorporating friction, wear, and lubrication processes within artificial joint systems are critical for comprehending their long-term performance, biocompatibility, and overall clinical success [42,43]. A unidirectional pin-on-disk (POD) tribometer was utilized in this test, where the pin made of 52,100 bearing steel and the disk made of 3D-printed PEEK, representing the joint components, were brought into contact, replicating loading, lubrication, and elliptical motions similar to those observed during the in vivo conditions of a prosthetic joint (Figure 2a).

The Vickers hardness indentation method was employed to estimate the hardness of the 3D-printed PEEK disks. A microhardness tester (Mitutoyo, Kawasaki, Japan) equipped with a square-base diamond pyramid indenter was used, applying a load (P) of 25 [gf] for 10 [s]. The indentation area was determined by measuring the average impression diagonal length of five points on the samples (d = 23 ± 2 µm). The average Vickers hardness number was calculated based on ASTM E384, and was determined to be 87 $\left[\text{Kgfmm}^{-2}\right]$ or 853 MPa.

The 3D-printed PEEK disks were meticulously cleaned before each test. Surface profilometry was conducted to measure the surface roughness of the 3D-printed disks in accordance with ASTM recommendations, requiring examination using a profilometer before the wear test. Atomic Force Microscopy (AFM) with a 2 pm diamond tip (JPK-NanoWizard® II, Berlin, Germany) was used to scan random points on the disk's surface. The results ranged from a roughness of Ra 0.028 µm and RMS 0.034 µm to a roughness of Ra 0.027 µm and RMS 0.034 µm.

3.2.1. Friction

The coefficients of friction (COFs) between the specimens as a function of the sliding distance obtained from the wear tests, which were carried out under 14, 30, 50, and 70 N at a temperature of 37 °C in FBS, are shown in Figure 3a.

The mean COF values of the samples were generally found to increase with increasing the applied load. Although surface asperities and orientation play crucial roles in reciprocating sliding, bulk mechanical properties have more effects on the coefficient of friction than surface roughness at higher loads. A high contact load and ploughing of the asperities cause plastic deformation and surface layer detachment of the 3D-printed PEEK polymer, resulting in higher apparent COF values at higher loads [44]. Third-body particles entrapped between the pin and the surface can also act as an abrasive and increase these COF values, the general increasing trend of which can be seen in in the frictional behavior during the whole wear tests [45].

The wear behavior of ME PEEK may also be influenced by the formation and breaking of interfacial adhesive bonds, the removal of material due to scratching and fatigue, and the formation of cracks in surface regions [46]. The roughness of the 3D-Printed PEEK surface can be decreased, resulting from an increase in loads, which causes the flattening of asperities. Therefore, at higher loads, the higher frequency fluctuation of the COF with sliding distance decreased.
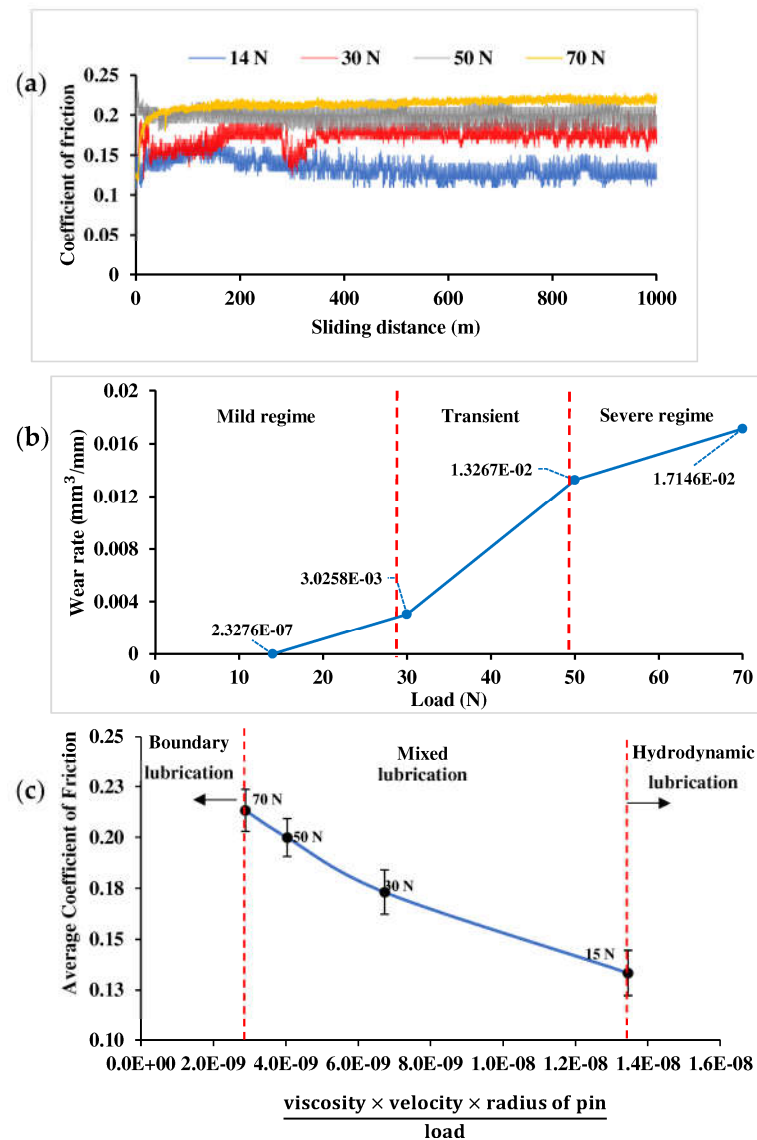
Figure 3. (**a**) Friction coefficient behavior of anti-friction 52,100 bearing steel and 3D-printed PEEK with respect to sliding distance in varying loads of 14, 30, 50, and 70 N. (**b**) Graph of wear rates as a function of the load identifying the dimensionless wear coefficient (K) for the different wear regimes. (**c**) Stribeck diagram illustrating the average coefficient of friction as a function of the Sommerfeld number characterized different regimes of lubrication.

During the wear test, the increased contact area could sustain a greater tangential force until the maximum shear stress of the material was reached. The COF continuously fluctuated due to adhesion and rupture asperity contacts [47]. Table 4 shows the mean COF values and the wear losses of the samples calculated after the 24 h wear test at various loads for better interpretation. It can be seen that both volumetric losses and the average of the COF values increased with increases in the applied load. It is believed that the penetration of the abrasive pin and wear debris on the samples increased by increasing the friction test load. However, in the process called densification, pre-existing pores in the 3D printed PEEK were filled with micron-sized wear particles under increased loads [48].

Table 4. Average coefficient of friction, Sommerfeld number, minimum film thickness, and Lambda factor determined by varying load from 14 to 70 N.

Load [N]	Average Coefficient of Friction	Sommerfeld Number	Minimum Fluid-Film Thickness [nm]	Lambda (λ)	Mass Loss [mg]	Specific Wear Rate [mm^{3}N^{-1}mm^{-1}]
14	0.133	1.34543×10^{-8}	1.887	0.018	0.30	1.66255×10^{-8}
30	0.173	6.72714×10^{-9}	1.608	0.015	3.90	1.00861×10^{-4}
50	0.200	4.03628×10^{-9}	1.444	0.014	17.10	2.65343×10^{-4}
70	0.213	2.88306×10^{-9}	1.346	0.013	22.10	2.44949×10^{-4}

3.2.2. Wear

In this work, where the pin was made of a hard metal material and the disk was made of a soft polymer material, the adhesive wear mechanism was dominant, as a consequence of the plastic deformation of the polymer's asperities [49,50].

Plotting the wear rate against the load, based on the experimental data obtained during pin-on-disc tests, with normal loads ranging from 14 to 70 N (Figure 3b), obtained a wear coefficient (K) increasing from 1.418×10^{-5} to 2.089×10^{-1} with the applied load, indicating a transition from mild to severe wear regimes. The normal load range from 14 N to 70 N was separated by an intermediate region spanning from 30 N to 50 N, illustrating the transition.

The specific wear rates (k) were determined to range from 1.66255×10^{-8} to 2.44949×10^{-4} $\left[\text{m}^3\text{N}^{-1}\text{m}^{-1}\right]$ based on varying the loads from 14 to 70 N (Table 4).

3.2.3. Lubrication

In situations where the applied load due to joint articulation becomes too high or there is low relative motion, fluid film lubrication becomes inadequate to sustain the load. This leads to the surface roughness surpassing the gap between the surfaces, resulting in the contact of asperities present on the surfaces, thus, the likely failure of the joint.

The Stribeck diagram was utilized to evaluate the lubrication regime by plotting the coefficient of friction against the Sommerfeld number, which takes into account the load, relative velocity of the disk, lubricant viscosity, and the pin's radius, as indicated in Equation (10) [51].

As the Sommerfeld number increased, the coefficient of friction exhibited distinct responses, where the boundary, mixed, and hydrodynamic regimes correspond to constant, reduced, and increased coefficients of friction, respectively [52].

$$Sommerfeld\ number = \frac{viscosity \times velocity \times radius\ of\ pin}{load} = \frac{\eta u R_{Pin}}{P} \tag{10}$$

When using FBS as the lubricant, its kinematic viscosity was measured to be 1.3 centistokes [cSt] at 40 °C and one-atmosphere pressure, as evaluated with an Ostwald viscometer. The viscosity was 1.339 $\left[\text{Nsm}^{-2}\right]$ based on its 1.03 $\left[\text{gml}^{-1}\right]$ density [41,53].

The wear assessment involved a constant sliding velocity of 120 rpm with a 4 mm radius of the wear track (corresponding to 0.0503 ms^{-1}) and a 3 mm radius of the pin. These parameters were chosen to closely resemble the articulating velocity between joints, which typically varies from 0 to 0.055 ms^{-1} [54]. Throughout the tribology experiments, all parameters remained constant, except for the load, which varied from 14 N to 70 N. From Figure 3c, it can be inferred that, as the Sommerfeld number increased due to declining loads, the coefficient of friction decreased, indicating the presence of mixed lubrication [52,55]. As a result, this region lay between the boundary and hydrodynamic regimes, illustrating that the loads were carried by both modes of lubrication. This phenomenon is akin to the lubrication of human joints, which have a low geometrical conformity [56].

This result also confirms another assumption used to assess the lubrication regimes, which states that full fluid film lubrication occurs only when the fluid film thickness exceeds the average roughness of the articulating surfaces by at least three times, preventing direct contact between asperities [51,57]. The fluid film thickness can be determined by considering the elastic deformation of the bearing materials and the viscosity of the lubricant, both of which have an impact on the lubrication regime.

In the tribology system where a hard metal pin articulates against a soft polymer with FBS as the lubricant, the isoviscous–elastic regime, also known as the EHL of low-elastic-modulus materials, is more likely to occur. This is due to the combination of the low elastic modulus of the 3D-printed PEEK material and the low viscosity of the FBS, resulting in the lowest pressure within the lubricant, similar to the conditions of dry friction. It is proposed that healthy joints, lubricated by the synovial fluid, can be simulated using the isoviscous–elastic regime. This is achievable due to the low viscosity of synovial fluid and the lower elastic modulus of joints compared to metals. The main objective is to measure the minimum film thickness under these simulated conditions, resembling the lubrication observed in healthy joints lubricated by synovial fluid [58].

The minimum EHL film thickness can be determined by computing the numerical results using Equations (11) and (12).

$$h_{min} = H_{min} \times R_x \tag{11}$$

$$\begin{cases} H_{min} = 7.43 U^{0.65} W^{-0.21} \left(1 - 0.85 e^{-0.31k}\right) \\ U = \frac{u\eta_0}{E'' R_x} \\ W = \frac{F}{E'' R_x^2} \\ u = r' \times \omega \\ \frac{1}{R_x} = \frac{1}{R_{Pin_x}} + \frac{1}{R_{disk_x}} \\ k = 1.03 \left(\frac{R_y}{R_x}\right)^{0.64} \end{cases} \tag{12}$$

The dimensionless film thickness (H-min) can be obtained using Equation (12), where W represents the dimensionless load parameter, η_0 is the fluid viscosity at a one-atmosphere pressure, u is the mean surface velocity in the x-direction, r' is the radius of stroke, ω is the angle velocity, U is the dimensionless speed parameter, k is the ellipticity parameter, F is the normal applied load, and R is the effective radius.

The ratio between the minimum film thickness and the surface roughness of asperities, denoted as the Lambda value (λ), could serve as an indicator for predicting which lubrication regimes will occur according to Equation (13) [51].

$$\lambda = \frac{h_{min}}{\left(Rq_{pin}^2 + Rq_{disk}^2\right)^{1/2}} \tag{13}$$

where Rq_{pin} and Rq_{disk} are the Root-Mean-Square (RMS) roughness values for each surface.

Therefore, fluid film lubrication predominates when $\lambda > 3$; however, for $\lambda < 3$, some load is carried by the fluid film, and some is supported by the solid-to-solid contact [59]. The Sommerfeld number, minimum fluid film thickness, Lambda, and specific wear rates are shown in Table 4.

3.2.4. Wear Mechanisms

Wear mechanisms were investigated by the SEM surface views of the 3D-printed PEEK samples which were obtained after the wear test carried out under (a) 14, (b) 30, (c) 30, and (d) 70 N static loading, as shown Figure 4. Considering the significant difference in hardness between the steel balls and PEEK, coupled with cyclic loading, the predominant failure mode in the 3D-printed PEEK samples could potentially stem from fretting and

fatigue effects. Moreover, the principal wear mechanism is likely to involve adhesion, as indicated by the presence of wear debris and surface smearing, which are clear signs of adhesive wear mechanisms. Plastic deformations in 3D-printed PEEK material are likely to manifest under both normal axial loads and shear loads during the initial stages of the sliding process [60]. The worn surface of the sample treated under a 14 N load, as shown in Figure 4a, displayed minimal plastic deformation, evident from the visible deposited raster.
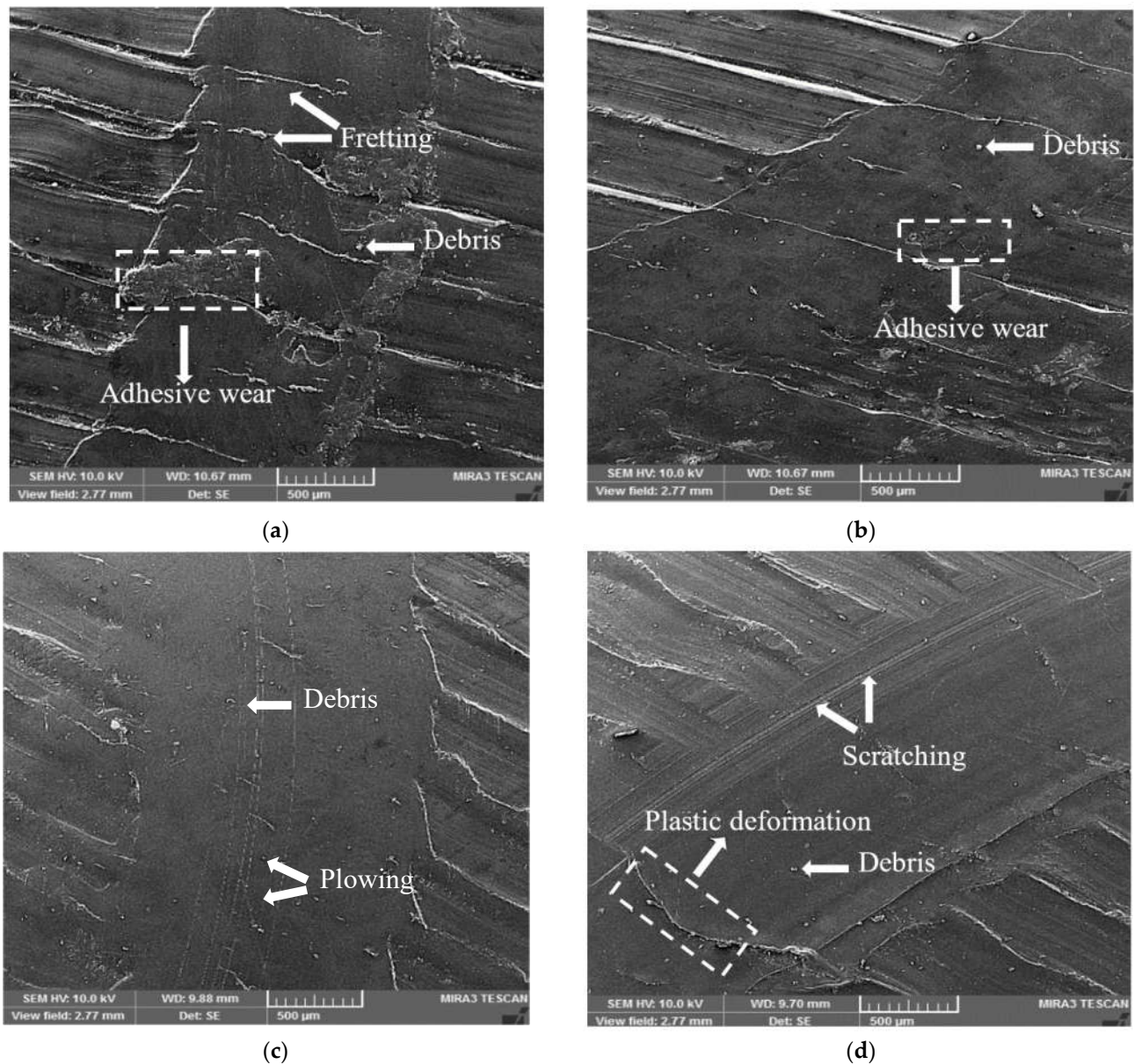
Figure 4. FE-SEM images of worn surfaces of the 3D-printed PEEK disks penetrated with different loads (**a**) 14 N, (**b**) 30 N, (**c**) 50 N, and (**d**) 70 N.

It appears that these deposited rasters did not undergo complete destruction under the 14 N load. It can be inferred, therefore, that the predominant wear mechanism was fretting wear. In fretting wear, the minimal relative motion between contacting surfaces results in localized wear without significant material removal [61]. The partial integrity of the surface rasters indicates a limited, localized damage characteristic of fretting rather than complete wear-out. As the applied load was increased to 30 N, there was a notable increase in plastic deformation, as shown in Figure 4b. This can result in the generation of submicron wear debris and the formation of wear cracks. Fretting wear is thought to

induce stress concentrations within the material, rendering components more vulnerable to fatigue failure [62]. The presence of submicron wear debris, along with the development of wear cracks and plastic deformations in the PEEK material, contributes to the formation of a polymer transfer film on the surface of the steel ball.

The deposited rasters subjected to a 30 N load displayed more pronounced signs of damage when compared to those depicted in Figure 4a subjected to 14 N. Under this load, the prevailing wear mechanism transitioned to adhesive wear. Figure 4c,d illustrate the worn surfaces of the sample treated under 50 N and 70 N loads, respectively. It can be seen that, in both conditions, the deposited rasters were removed. In addition, some plowing or scratching can be observed. The plowing action initiates significant plastic deformation in the PEEK material [60,63], generating wear particles during the cyclic reciprocating shearing process inherent to PEEK. These wear particles, comprising PEEK polymer, adhere to the steel ball due to elevated frictional heat and substantial contact pressure. Consequently, this adhesion of 3D-printed PEEK debris can lead to a combination of adhesion and abrasion mechanisms, which can synergistically amplify the overall wear process characterized by extensive material removal and transfer. As a result, 3D-printed PEEK experiences its most accelerated wear rate under severe adhesive wear conditions when subjected to high loads. Therefore, it can be concluded that the prevailing wear and failure mechanisms at 50 N and 70 N loads are primarily associated with plastic deformation and fatigue wear, occurring within the context of reciprocating plowing and scratching processes.

In addition, it can be inferred that there is a relationship between applied load and the mechanical behavior of additively manufactured PEEK. Specifically, as the load increased, both the coefficient of friction and wear rates exhibited a corresponding rise, suggesting that heightened contact pressure enhances material removal. Additionally, contact pressure itself increased with load, further contributing to the wear mechanisms observed. The lubrication regimes transitioned from mild at lower loads to severe at higher loads, emphasizing the critical role of effective lubrication in mitigating wear. Notably, the thickness of the lubrication film decreased with increasing loads, which can compromise the protective barrier and exacerbate surface contact. The wear mechanisms transitioned from predominantly minimal plastic deformation and fretting wear at lower loads to significant plastic deformations, wear crack formation, and adhesive wear at higher loads. These observations are supported by Sthe EM analysis, which revealed significant wear patterns correlating with increased loads and changing lubrication conditions. This comprehensive understanding of the interplay between load, friction, lubrication, contact pressure, and wear mechanisms provides essential insights for optimizing the performance of additively manufactured PEEK in prosthetic applications.

4. Conclusions

In considering the mechanical anisotropy and tribological aspects of the ME of implant-grade PEEK, the following conclusions can be reached:

(1) When subjected to loading perpendicular to the layer direction, the PEEK samples exhibited an elastic modulus of 2.30 ± 0.10 GPa and a yield strength of 61.0 ± 1.0 MPa. Conversely, when loaded parallel to the layer direction, the samples demonstrated an elastic modulus of 2.30 ± 0.2 GPa and a yield strength of 76.0 ± 7.0 MPa. The mean Young's modulus of (2.505 GPa) can be attributed to the application of both normal and tangential loads during the pin-on-disk test.

(2) In 3D-printed PEEK, the onset of elastic-plastic and fully plastic deformation occurred when the mean contact pressure reached approximately 1.064 times the material's yield strength. In contrast to metals, where a distinct transition between the elastic–plastic and fully plastic regions is typically observed at around 2.8 times the yield strength, the 3D-printed PEEK did not exhibit a clear separation between these deformation phases.

(3) The wear coefficients (K) for 3D-printed PEEK material were calculated values of 1.418×10^{-5} and 2.089×10^{-1} under mild and severe wear conditions, respectively.

(4) A mixed lubrication mechanism was determined through the Stribeck curve, which highlighted a decrease in the average coefficient of friction as the Sommerfeld number increased. Mmixed lubrication is suggested by the ratio between the minimum film thickness and the surface roughness being less than 3 for all applied loads.

(5) The COF increased with load due to complex interplay of factors influencing frictional behavior.

(6) Increasing the applied load led to varying wear mechanisms in the 3D-printed PEEK, progressing from minimal plastic deformation and fretting wear at lower loads to pronounced plastic deformations, wear crack formation, and adhesive wear at higher loads.

This study has significant implications for the design of additively manufactured PEEK prostheses for artificial joint arthroplasty. PEEK's non-biodegradable nature and elastic modulus, which is closer to that of bone than metals, make it a promising material for joint replacements. By providing insights into wear rates, friction coefficients, and lubrication regimes under conditions similar to articular joints, this research can guide the tailored design of customized prostheses. Additionally, it highlights the importance of the anisotropic properties of 3D-printed PEEK, as these influence its mechanical and tribological performance in artificial joint applications.

Author Contributions: Conceptualization, M.R.M.; methodology, M.R.M., M.R.N., T.S. and M.M.; validation, M.R.M. and M.R.N.; investigation, M.R.M. and M.R.N.; writing—original draft, M.R.M.; writing—review and editing, M.R.M., M.R.N., T.S. and M.M.; visualization, M.R.M.; supervision, T.S. and M.M. All authors have read and agreed to the published version of the manuscript.

References

1. Hunter, D.J.; March, L.; Chew, M. Osteoarthritis in 2020 and beyond: A Lancet Commission. *Lancet* **2020**, *396*, 1711–1712. [CrossRef] [PubMed]
2. Glyn-Jones, S.; Palmer, A.J.; Agricola, R.; Price, A.J.; Vincent, T.L.; Weinans, H.; Carr, A.J. Osteoarthritis. *Lancet* **2015**, *386*, 376–387. [CrossRef] [PubMed]
3. Fu, K.; Robbins, S.R.; McDougall, J.J. Osteoarthritis: The genesis of pain. *Rheumatology* **2018**, *57*, iv43–iv50. [CrossRef] [PubMed]
4. Rassir, R.; Nellensteijn, J.M.; Saouti, R.; Nolte, P.A. Bilateral massive osteolysis of uncertain origin after total knee arthroplasty: A case report and review of literature. *Int. J. Surg. Case Rep.* **2021**, *80*, 105678. [CrossRef] [PubMed]
5. Binkley, N.; Nickel, B.; Anderson, P.A. Periprosthetic fractures: An unrecognized osteoporosis crisis. *Osteoporos. Int.* **2023**, *34*, 1055–1064. [CrossRef]
6. Zhang, X.; Zhang, Y.; Jin, Z. A review of the bio-tribology of medical devices. *Friction* **2022**, *10*, 4–30. [CrossRef]
7. Au, A.G.; Raso, V.J.; Liggins, A.B.; Amirfazli, A. Contribution of loading conditions and material properties to stress shielding near the tibial component of total knee replacements. *J. Biomech.* **2007**, *40*, 1410–1416. [CrossRef]
8. Unsworth, A.; Scholes, S.C.; Smith, S.L.; Elfick, A.P.D.; Ash, H.A. Tribology of replacement hip joints. In *Tribology Series*; Elsevier: Amsterdam, The Netherlands, 2000; pp. 195–202.
9. Golish, S.R.; Anderson, P.A. Bearing surfaces for total disc arthroplasty: Metal-on-metal versus metal-on-polyethylene and other biomaterials. *Spine J.* **2012**, *12*, 693–701. [CrossRef]
10. Mont, M.A.; Booth, R.E., Jr.; Laskin, R.S.; Stiehl, J.B.; Ritter, M.A.; Stuchin, S.A.; Rajadhyaksha, A.D. The spectrum of prosthesis design for primary total knee arthroplasty. *Instr. Course Lect.* **2003**, *52*, 397–407.
11. Clarke, I.C.; Manaka, M.; Green, D.D.; Williams, P.; Pezzotti, G.; Kim, Y.-H.; Ries, M.; Sugano, N.; Sedel, L.; Delauney, C.; et al. Current status of zirconia used in total hip implants. *JBJS* **2003**, *85*, 73–84. [CrossRef]
12. Maydanshahi, M.R.; Nazarian, A.; Eygendaal, D.; Ebrahimzadeh, M.H.; Kachooei, A.R.; Mousavi Shaegh, S.A. 3D printing-assisted fabrication of a patient-specific antibacterial radial head prosthesis with high periprosthetic bone preservation. *Biomed. Mater.* **2021**, *16*, 035027. [CrossRef] [PubMed]

13. Wang, A.; Lin, R.; Stark, C.; Dumbleton, J.H. Suitability and limitations of carbon fiber reinforced PEEK composites as bearing surfaces for total joint replacements. *Wear* **1999**, *225–229*, 724–727. [CrossRef]

14. Grupp, T.M.; Meisel, H.-J.; Cotton, J.A.; Schwiesau, J.; Fritz, B.; Blömer, W.; Jansson, V. Alternative bearing materials for intervertebral disc arthroplasty. *Biomaterials* **2010**, *31*, 523–531. [CrossRef] [PubMed]

15. Katzer, A.; Marquardt, H.; Westendorf, J.; Wening, J.V.; Von Foerster, G. Polyetheretherketone—Cytotoxicity and mutagenicity in vitro. *Biomaterials* **2002**, *23*, 1749–1759. [CrossRef] [PubMed]

16. Graham, J.; Peck, J. Chapter 26—FDA Regulation of PEEK Implants☆ . In *PEEK Biomaterials Handbook*, 2nd ed.; Kurtz, S.M., Ed.; William Andrew Publishing: Norwich, NY, USA, 2019; pp. 431–445. [CrossRef]

17. Wang, Y.; Müller, W.D.; Rumjahn, A.; Schwitalla, A. Parameters Influencing the Outcome of Additive Manufacturing of Tiny Medical Devices Based on PEEK. *Materials* **2020**, *13*, 466. [CrossRef]

18. Solomon, I.J.; Sevvel, P.; Gunasekaran, J. A review on the various processing parameters in FDM. *Mater. Today Proc.* **2020**, *37*, 509–514. [CrossRef]

19. Cai, W.; Trefs, J.L.; Hugel, T.; Balzer, B.N. Anisotropy of π-πStacking as Basis for Superlubricity. *ACS Mater. Lett.* **2023**, *5*, 172–179. [CrossRef]

20. Cai, W.; Bullerjahn, J.T.; Lallemang, M.; Kroy, K.; Balzer, B.N.; Hugel, T. Angle-dependent strength of a single chemical bond by stereographic force spectroscopy. *Chem. Sci.* **2022**, *13*, 5734. [CrossRef]

21. Cai, W.; Jäger, M.; Bullerjahn, J.T.; Hugel, T.; Wolf, S.; Balzer, B.N. Anisotropic Friction in a Ligand-Protein Complex. *Nano Lett.* **2023**, *23*, 4111–4119. [CrossRef]

22. Arif, M.F.; Kumar, S.; Varadarajan, K.M.; Cantwell, W.J. Performance of biocompatible PEEK processed by fused deposition additive manufacturing. *Mater. Des.* **2018**, *146*, 249–259. [CrossRef]

23. Vaezi, M.; Yang, S. Extrusion-based additive manufacturing of PEEK for biomedical applications. *Virtual Phys. Prototyp.* **2015**, *10*, 123–135. [CrossRef]

24. Wang, Y.; Müller, W.-D.; Rumjahn, A.; Schmidt, F.; Schwitalla, A.D. Mechanical properties of fused filament fabricated PEEK for biomedical applications depending on additive manufacturing parameters. *J. Mech. Behav. Biomed. Mater.* **2021**, *115*, 104250. [CrossRef] [PubMed]

25. Arif, M.F.; Alhashmi, H.; Varadarajan, K.M.; Koo, J.H.; Hart, A.J.; Kumar, S. Multifunctional performance of carbon nanotubes and graphene nanoplatelets reinforced PEEK composites enabled via FFF additive manufacturing. *Compos. Part B Eng.* **2020**, *184*, 107625. [CrossRef]

26. Zhang, X.; Hu, Y.; Chen, K.; Zhang, D. Bio-tribological behavior of articular cartilage based on biological morphology. *J. Mater. Sci. Mater. Med.* **2021**, *32*, 132. [CrossRef]

27. Howling, G.I.; Sakoda, H.; Antonarulrajah, A.; Marrs, H.; Stewart, T.D.; Appleyard, S.; Rand, B.; Fisher, J.; Ingham, E. Biological Response to Wear Debris Generated in Carbon Based Composites as Potential Bearing Surfaces for Artificial Hip Joints. *J. Biomed. Mater. Res. Part B Appl. Biomater.* **2003**, *67*, 758–764. [CrossRef]

28. Liaw, C.Y.; Tolbert, J.W.; Chow, L.W.; Guvendiren, M. Interlayer bonding strength of 3D printed PEEK specimens. *Soft Matter* **2021**, *17*, 4775–4789. [CrossRef]

29. Rahman, K.M.; Letcher, T.; Reese, R. Mechanical properties of additively manufactured peek components using fused filament fabrication. *ASME Int. Mech. Eng. Congr. Expo. Proc.* **2015**, *57359*, V02AT02A009. [CrossRef]

30. Chacón, J.M.; Caminero, M.A.; García-Plaza, E.; Núñez, P.J. Additive manufacturing of PLA structures using fused deposition modelling: Effect of process parameters on mechanical properties and their optimal selection. *Mater. Des.* **2017**, *124*, 143–157. [CrossRef]

31. Pohrt, R.; Popov, V.L.; Pastewka, L.; Robbins, M.O.; Greenwood, J.A.; Tripp, J.H.; Hui, C.Y.; Liu, T.; Salez, T.; Raphael, E.; et al. Fused filament fabrication of peek: A review of process-structure-property relationships. *Polymers* **2021**, *12*, 1665. [CrossRef]

32. Gao, X.; Qi, S.; Kuang, X.; Su, Y.; Li, J.; Wang, D. Fused filament fabrication of polymer materials: A review of interlayer bond. *Addit. Manuf.* **2021**, *37*, 101658. [CrossRef]

33. Hearmon, R.F.S. The elastic constants of anisotropic materials—II. *Adv. Phys.* **1956**, *5*, 323–382. [CrossRef]

34. Kim, D.-H. Composite Structures for Civil and Architectural Engineering. In *Composite Structures for Civil and Architectural Engineering*; CRC Press: London, UK, 1994. [CrossRef]

35. Popov, V.L.; Heß, M.; Willert, E. *Handbook of Contact Mechanics*; Springer: Berlin/Heidelberg, Germany, 2019. [CrossRef]

36. Nejati, M.; Dambly, M.L.T.; Saar, M.O. A methodology to determine the elastic properties of anisotropic rocks from a single uniaxial compression test. *J. Rock Mech. Geotech. Eng.* **2019**, *11*, 1166–1183. [CrossRef]

37. WEI, D.; ZHAI, C.; HANAOR, D.; GAN, Y. Contact behaviour of simulated rough spheres generated with spherical harmonics. *Int. J. Solids Struct.* **2020**, *193–194*, 54–68. [CrossRef]

38. Stronge, W.J. *Continuum Modeling for Local Deformation Near Contact Area*; Cambridge University Press: Cambridge, UK, 2018. [CrossRef]

39. Fundamentals, S. *Encyclopedia of Tribology*; Elsevier: Amsterdam, The Netherlands, 2013. [CrossRef]

40. Tabor, D. The hardness of solids. *Rev. Phys. Technol.* **1970**, *1*, 145–179. [CrossRef]

41. Hutchings, I.M. Tribology: Friction and wear of engineering materials. *Mater. Des.* **1992**, *13*, 187. [CrossRef]

42. Walker, P.S.; Gold, B.L. The tribology (friction, lubrication and wear) of all-metal artificial hip joints. *Wear* **1971**, *17*, 285–299. [CrossRef]

43. Sahoo, P.; Das, S.K.; Paulo Davim, J. *Tribology of Materials for Biomedical Applications*; Elsevier Ltd.: Amsterdam, The Netherlands, 2019. [CrossRef]

44. Dangnan, F.; Espejo, C.; Liskiewicz, T.; Gester, M.; Neville, A. Friction and wear of additive manufactured polymers in dry contact. *J. Manuf. Process.* **2020**, *59*, 238–247. [CrossRef]

45. Najari, M.R.; Sajjadi, S.A.; Ganji, O. Microstructural evolution and wear properties of chromium carbide coating formed by thermo-reactive diffusion (TRD) process on a cold-work tool steel. *Results Surf. Interfaces* **2022**, *8*, 100059. [CrossRef]

46. Equbal, A.; Sood, A.K.; Toppo, V.; Ohdar, R.K.; Mahapatra, S.S. Prediction and analysis of sliding wear performance of fused deposition modelling-processed ABS plastic parts. *Proc. Inst. Mech. Eng. Part J J. Eng. Tribol.* **2010**, *224*, 1261–1271. [CrossRef]

47. Günen, A.; Kalkandelen, M.; Gök, M.S.; Kanca, E.; Kurt, B.; Karakaş, M.S.; Karahan, İ.H.; Çetin, M. Characteristics and high temperature wear behavior of chrome vanadium carbide composite coatings produced by thermo-reactive diffusion. *Surf. Coat. Technol.* **2020**, *402*, 126402. [CrossRef]

48. Betancourt-Dougherty, L.C.; Smith, R.W. Effects of load and sliding speed on the wear behaviour of plasma sprayed TiC NiCrBSi coatings. *Wear* **1998**, *217*, 147–154. [CrossRef]

49. Gang, S.; Fengzhou, F.; Chengwei, K. Tribological Performance of Bioimplants: A Comprehensive Review. *Nami Jishu Yu Jingmi Gongcheng/Nanotechnol. Precis. Eng.* **2018**, *1*, 107–122. [CrossRef]

50. Walczak, M.; Caban, J. Tribological characteristics of polymer materials used for slide bearings. *Open Eng.* **2021**, *11*, 624–629. [CrossRef]

51. Unsworth, A. Tribology of artificial hip joints. *Proc. Inst. Mech. Eng. Part J J. Eng. Tribol.* **2006**, *220*, 711–718. [CrossRef]

52. Shen, G.; Zhang, J.F.; Fang, F.Z. In vitro evaluation of artificial joints: A comprehensive review. *Adv. Manuf.* **2019**, *7*, 1–14. [CrossRef]

53. Hamrock, B.J.; Schmid, S.R.; Jacobson, B.O. Fundamentals of Fluid Film Lubrication. In *Fundamentals of Fluid Film Lubrication*; CRC Press: Boca Raton, FL, USA, 2004. [CrossRef]

54. Streicher, R.M. Tribology of Artificial Joints. In *Endoprosthetics*; Springer: Berlin/Heidelberg, Germany, 1995; pp. 34–48. [CrossRef]

55. Unswotih, A. Recent developments ology of artificial in the joints. *Tribol. Int.* **1995**, *28*, 485–495. [CrossRef]

56. Unsworth, A. Tribology of human and artificial joints. *Proc. Inst. Mech. Eng. Part H J. Eng. Med.* **1991**, *205*, 163–172. [CrossRef]

57. Yan, Y. Tribology and tribo-corrosion testing and analysis of metallic biomaterials. In *Metals for Biomedical Devices*; Woodhead Publishing: Cambridge, UK, 2010; pp. 178–201. [CrossRef]

58. Dowson, B.J.; Dowson, D. *Minimum Film Thickness in Elliptical Contacts for Different Regimes of Fluid-Film Lubrication*; NASA Technical Paper 1342; NASA: Washington, DC, USA, 1978.

59. Stewart, T.D. Tribology of artificial joints. *Orthop. Trauma* **2010**, *24*, 435–440. [CrossRef]

60. Wang, S.; Song, J.; Liao, Z.; Liu, Y.; Zhang, C.; Liu, W. Study on the Wettability and Tribological Behavior of Different Polymers as Bearing Materials for Cervical Prosthesis. *J. Mater. Eng. Perform.* **2015**, *24*, 2481–2493. [CrossRef]

61. Guo, Q.; Luo, W. Mechanisms of fretting wear resistance in terms of material structures for unfilled engineering polymers. *Wear* **2001**, *249*, 924–931. [CrossRef]

62. Jin, X.; Shipway, P.H.; Sun, W. The Role of Temperature and Frequency on Fretting Wear of a Like-on-Like Stainless Steel Contact. *Tribol. Lett.* **2017**, *65*, 77. [CrossRef]

63. Massocchi, D.; Riboni, G.; Lecis, N.; Chatterton, S.; Pennacchi, P. Tribological Characterization of Polyether Ether Ketone (PEEK) Polymers Produced by Additive Manufacturing for Hydrodynamic Bearing Application. *Lubricants* **2021**, *9*, 112. [CrossRef]